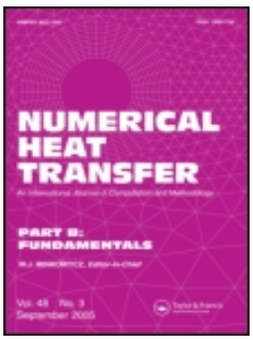

Taylor & Francis
Taylor & Francis Group

Numerical Heat Transfer, Part B: Fundamentals
An International Journal of Computation and Methodology

ISSN: 1040-7790 (Print) 1521-0626 (Online) Journal homepage: http://www.tandfonline.com/loi/unhb20

A New Numerical Approach for Predicting the Two-Phase Flow of Refrigerants during Evaporation and Condensation

I. Fayssal & F. Moukalled

To cite this article: I. Fayssal & F. Moukalled (2012) A New Numerical Approach for Predicting the Two-Phase Flow of Refrigerants during Evaporation and Condensation, Numerical Heat Transfer, Part B: Fundamentals, 62:5, 341-369, DOI: 10.1080/10407790.2012.707009

To link to this article: http://dx.doi.org/10.1080/10407790.2012.707009

Numerical Heat Transfer, Part B, 62: 341–369, 2012

ISSN: 1040-7790 print/1521-0626 online
DOI: 10.1080/10407790.2012.707009

Taylor & Francis
Taylor & Francis Group

A NEW NUMERICAL APPROACH FOR PREDICTING THE TWO-PHASE FLOW OF REFRIGERANTS DURING EVAPORATION AND CONDENSATION

I. Fayssal and F. Moukalled
Department of Mechanical Engineering, American University of Beirut, Beirut, Lebanon

This article reports on four finite-volume–based numerical methods developed for predicting the one-dimensional two-phase flow of pure refrigerants in evaporators and condensers during change-of-phase processes. The methods differ in the physical assumptions considered at the interface separating the liquid and vapor phases and in the equation used to predict the variation of the refrigerant flow quality during change of phase. In all methods, numerical predictions are obtained via a locally iterative marching-type solution algorithm. Therefore, the models permit the prediction of the size of the pipe needed to achieve full evaporation/condensation of the saturated refrigerant. The effectiveness and robustness of the numerical procedures in predicting the flow and heat transfer characteristics are assessed by comparing results with published experimental data. Good agreement is obtained. The new approach is used to perform a parametric study analyzing the effect of refrigerant type, pipe diameter, and mass flow rate on the flow and heat transfer characteristics in evaporators.

INTRODUCTION

Evaporator and condenser coils consist of a network of pipes whose primary function is to efficiently transfer heat between two media. Therefore a thorough understanding of the two-phase flow features and evaporation/condensation heat transfer characteristics of refrigerants in pipes is a prerequisite to properly designing these coils.

This study reports on the prediction of hydrodynamic and thermal fields of pure refrigerants in evaporators and condensers, which are modeled as horizontal circular pipes. The annular flow is considered to be the dominating flow regime of the liquid and vapor phases during the change-of-phase process. Two different formulations of the flow quality are developed, which account for the drop in pressure due to inertial and frictional effects.

Several methods have been developed to predict the change-of-phase phenomena arising in a variety of situations. Guo et al. [1] presented a numerical technique

Received 14 February 2012; accepted 16 April 2012.
The financial support provided by the University Research Board (URB) of the American University of Beirut is gratefully acknowledged.
Address correspondence to F. Moukalled, Department of Mechanical Engineering, American University of Beirut, P.O. Box 11-0256, Riad El-Solh, Beirut 1107 2020, Lebanon. E-mail: memouk@aub.edu.lb

NOMENCLATURE

A	pipe cross-sectional area, m^2	Re	Reynolds number
Bo	boiling number	T	temperature, K
C_p	specific heat capacity at constant pressure, J/kg K	V	velocity, m/s
		x	parameter in axial direction
C_v	specific heat capacity at constant volume, J/kg K	x_f	flow quality
		(X)	Lockhart-Martinelli parameter
$[dP/dz]$	pressure gradient, N/m^2	y	parameter in vertical direction
dS	surface derivative	α	volume fraction
dx	differential along x direction	α_T	volumetric coefficient of thermal expansion, K^{-1}
Di	heat exchanger inner diameter, m		
D_{vap}	vapor core diameter, m	β	coefficient of compressibility, Pa^{-1}
f	friction factor	δ_t	liquid film thickness, m
g	gravitational acceleration, m/s^2	ΔP	differential pressure, Pa
G_R	total mass flux, $kg/m^2\,s$	ε	tube roughness, m
h_{fc}	single-phase liquid heat transfer coefficient, W/m^2 K	μ	dynamic viscosity, Pa s
		v	specific volume, $m^3/$ kg
h_{int}	heat transfer coefficient at inner wall, W/m^2 K	ρ	density, kg/m^3
		σ	surface tension, N/m
h_v	convective vapor heat transfer coefficient, W/m^2 K	τ	wall shear stress, N/m^2
		ϕ_{lo}	two-phase frictional multiplier
i, h	specific enthalpy, total enthalpy, J/kg	**Subscripts**	
i_{fg}	heat of vaporization, J/kg	(f)	control-volume face
k	thermal conductivity, W/m^2 K	i	interfacial
$\dot{m}$	mass flow rate, kg/s	l	liquid
$\dot{M}$	mass transfer rate per unit volume, $kg/m^3\,s$	lo	total mass flux flowing with liquid properties only
$\vec{n}$	unit vector normal to surface	s	sensible
P	pressure, Pa	sat	saturation
Pr	Prandtl number	v	vapor
Q, Q_w	heat, W; heat flux, W/m^2	vo	total mass flux flowing with vapor properties only
$\dot{Q}$	volumetric flow rate, m^3/s		

to simulate flows with changes of phase using the volume-of-fluid level set (VOSET) method for interface tracking. The developed procedure was employed to solve several problems including the boiling of a horizontal film of water at near critical pressure. Maurya et al. [2] used a finite-volume–based incompressible flow algorithm to simulate the evaporating flow of a two-dimensional laminar developing film falling over an inclined plane surface, subjected to a constant wall heat flux. The computed results showed that the evaporation of fluid begins only after the growing thermal boundary layer reaches the interface. Kunkelmann and Stephan [3] implemented a nucleate boiling model in the volume-of-fluid solver of Open FOAM and used it to simulate the sucking interface problem and the growth of a spherical bubble. Hu and Zhang [4] used a modified k–ε turbulence model for gas–liquid two-phase flows to simulate the heat transfer between steam vapor and cooling water in tube-and-shell condensers. Lee and Son [5] studied numerically the bubble dynamics and heat transfer associated with nucleate boiling in a micro channel. In their work, the liquid–vapor interface was tracked by a modified level set method which included

the effects of phase change and contact angle. Zhang et al. [6] investigated numerically the heat and mass transfer with condensation in porous media. A modeling experiment was conducted to partially validate the calculation. Louahlia-Gualous and Asbik [7] presented a mathematical formulation of forced-convection condensation of pure fluid and binary mixtures in pipes. The numerical algorithm was used to study the effects of tube diameter on several hydrodynamic and heat transfer parameters. Bin-Mansoor and Yilbas [8] employed a numerical method to predict temperature field and recessing velocities of evaporating and melting surfaces in the region irradiated by a laser beam. Louahlia and El Omari [9] reported on experimental, numerical, and inverse heat conduction (IHCP) analysis of the evaporation heat transfer of a falling liquid film on a horizontal cylinder. Asbik et al. [10] studied numerically the onset of transverse and longitudinal transitions between turbulent and laminar regimes during the evaporation of a water film and evaluated the effects of different turbulence models and the main parameters on the transition position.

Workers have used a variety of techniques to measure the flow quality in a two-phase flow. Abdul-Razzak et al. [11] formulated an empirical correlation relating the flow quality to the void fraction through the Lockhart-Martinelli parameter [12]. The correlation is applicable in the various two-phase flow regimes except bubbly flows and is valid for a flow quality between 0.01 and 0.91 and a mass flux between 78 and 670 $kg/m^2 s$. Solberg et al. [13] calculated the flow quality from energy conservation by heating a refrigerant in a calorimeter and measuring its exit temperature and pressure. A similar approach was adopted by Kim and O'Neal [14] to determine the flow quality of an HFC-1% a-PAG oil mixture. Sripattrapan and Wongwises [15] investigated the heat transfer and flow characteristics of refrigerants during evaporation in a horizontal tube by solving the set of governing conservation equations using Newton's method.

Many studies have reported on the heat transfer coefficients and pressure drops of refrigerants undergoing evaporation and condensation processes. An experimental investigation was conducted by Grecoa and Vanoli [16–18] to measure the heat transfer coefficient and pressure drop of pure and mixture-type refrigerants flowing in a smooth horizontal tube (6 mm I.D.,6 m in length) during evaporation. Their measured pressure gradients and heat transfer coefficients were compared with available pressure drop and heat transfer correlations reported in [19–25], respectively. Jong-Taek et al. [26] investigated the effect of mass flux, heat flux, saturation temperature, and inner tube diameter on the boiling heat transfer coefficient of five refrigerants flowing in horizontal tubes of small diameters. Yang et al. [27] investigated the boiling of R141b refrigerant when subjected to a uniform heat flux while flowing in a horizontal coiled tube. Simulations were conducted using the volume-of-fluid (VOF) multiphase flow model and validated experimentally. Dalkilic [28] studied experimentally the two-phase pressure drop characteristics of R410a, R502, and R507a during condensation in a horizontal tube-in-tube heat exchanger 3.81 m long. Measurements were compared with available data and correlations in the literature to find the best combination of experimental and predicted results. Bhramara et al. [29] examined numerically the frictional pressure drop of three refrigerants flowing in a horizontal tube during condensation at different operating conditions of saturation pressure and mass flow rate. Their study was performed using a commercial computational fluid dynamics (CFD) code with the two-phase flow modeled as a

pseudo-single phase with average properties expressed as functions of the flow quality. Granryd [30] formulated a relation to determine the optimum length of tubes to be used in evaporators, which depends on the refrigerant pressure drop and its physical properties.

In this article, solutions of the two-phase flow are limited to the region within the saturation curve, with the aim of predicting the flow characteristics in evaporators and condensers. While the majority of studies reported in the literature have investigated the characteristics of refrigerants during evaporation and condensation, relying greatly on existing correlations for pressure drop and heat transfer coefficients, the current work provides a broader solution methodology. The conservation equations are discretized using the control-volume method and the resulting algebraic equations are solved by implementing four different numerical approaches that are detailed in a later section. The performance of each approach is assessed in terms of accuracy and computational cost by solving several test problems.

PHYSICAL MODEL AND GOVERNING EQUATIONS

Schematics of the physical situation showing a side view of the pipe to be modeled and its cross-sectional area are depicted in Figure 1. The length of the pipe to be computed is designated by L, and its inner diameter is D_i. The current study is limited to investigating pure refrigerants flowing in the two-phase flow regime with the fluid saturation temperature assumed to be uniformly distributed and its variations affected only by pressure drop due to frictional and acceleration effects. The single-phase regions, including the superheated and subcooled zones of the refrigerant, are not modeled here; the hydrodynamic and thermal characteristics of the flow in the two-phase region are of more interest. The transition to different flow morphologies is not adopted, and the flow is considered to be of the annular type for the whole phase-change phenomenon, with liquid flowing in the area adjacent to the pipe wall and vapor in the core region. Therefore, the drag and lift terms between the phases are neglected in the momentum equation. Each phase is considered to possess its own velocity field, with an interface region occurring between the two phases without mixing (i.e., no liquid droplets exist in the core region and no vapor is present in the liquid film). The interaction between the liquid and vapor phases is considered to occur at the interface region separating them.

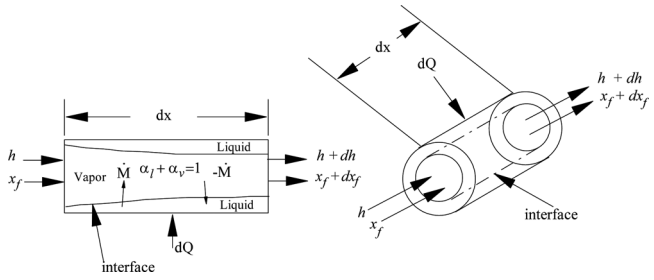

Figure 1. Schematic of a control volume showing the heat, volume fraction, and mass balance of the refrigerant constituents.

The mass transfer process at the liquid–vapor interface is modeled through the addition of mass source terms to the phasic continuity equations. The one-dimensional steady-state continuity equations for the vapor (v) and liquid (l) phases during evaporation are written as

$$\nabla.(\alpha_v \rho_v V_v) = \dot{M} \quad \text{and} \quad \nabla.(\alpha_l \rho_l V_l) = -\dot{M} \tag{1}$$

with $\dot{M}$ representing the source term accounting for the mass transfer rate per unit volume between the liquid and vapor phases. During condensation, the negative and positive signs of the source term in Eq. (1) are exchanged.

Since the liquid and vapor phases share the same pressure field, a combined momentum equation is obtained by adding the liquid and vapor phasic momentum equations, which is written in a vector form as

$$\nabla.(\alpha_l \rho_l V_l^2) + \nabla.(\alpha_v \rho_v V_v^2) = -\nabla.P + \frac{4}{D_i}\tau - \rho g\vec{j} \tag{2}$$

This momentum equation [Eq. (2)] is used to compute the pressure at any axial location (i.e., at the outlet face of a control volume). Drag between the two phases is not accounted for, because of the assumption that the liquid and vapor phases do not mix. Moreover, since a horizontal pipe is considered, the gravitational term appearing in Eq. (2) is dropped out.

Heat and Mass Transport

The conservation of energy equation can be written as

$$\frac{\partial(\alpha_v \rho_v V_v e_v)}{\partial z} + \frac{\partial(\alpha_l \rho_l V_l e_l)}{\partial z} = \frac{4}{D_i} Q_w \tag{3}$$

where Q_w is the heat flux at the pipe wall and e_l and e_v represent, respectively, the specific energies for the liquid and vapor phases, given by

$$e_l = i_l + \frac{V_l^2}{2} + gy \quad \text{and} \quad e_v = i_v + \frac{V_v^2}{2} + gy \tag{4}$$

However, instead of using the equation above, alternative forms of energy conservation are developed, as will be explained next.

Energy conservation over a control volume can be expressed in terms of the change of the refrigerant total enthalpy during change of phase (the state of the refrigerant varies between saturated liquid and saturated vapor) and in differential form is written as

$$dQ = \dot{m}|dh| \tag{5}$$

where dQ is the differential heat imposed at the wall of a control volume and $|dh|$ is the absolute differential enthalpy due to change of phase.

In modeling the flow and heat transfer at the core of the fluid, two different physical assumptions are investigated. In the first, the sensible heat transfer at the

liquid–vapor interface is set to zero. Therefore the liquid and vapor phases are assumed to possess the bulk saturation temperature of the refrigerant (i.e., $T_l = T_v = T_{\text{sat}}$), computed recursively in REFPROP [31].

In the second assumption, sensible heat transfer is assumed to occur at the liquid–vapor interface due to temperature gradient; therefore the liquid and vapor phases are at different temperatures (i.e., $T_l \neq T_v$). In this case, the temperatures of the liquid and vapor phases are established from the general relation between the specific heat capacities derived from Maxwell relations [32, 33] given, respectively, by

$$T_l = \left(C_{p,l} - C_{v,l}\right)\frac{\beta_l}{\alpha_{Tl}^2 v_l} \quad \text{and} \quad T_v = \left(C_{p,v} - C_{v,v}\right)\frac{\beta_v}{\alpha_{Tv}^2 v_v} \tag{6}$$

In the above equation, C_p and C_v represent the specific heat capacities at constant pressure and volume, respectively, α_T is the volumetric coefficient of thermal expansion; and β is the coefficient of compressibility. α_T and β are defined, respectively, as

$$\alpha_T = \frac{1}{v}\left(\frac{\partial v}{\partial T}\right)_P \quad \text{and} \quad \beta = -\frac{1}{v}\left(\frac{\partial v}{\partial P}\right)_T \tag{7}$$

Due to the low thermal conductivity of the vapor and liquid phases, the conductance between the two phases is neglected. Hence, convection is assumed to be the dominant heat transfer mode accounting for the transport of sensible heat between the two phases. Therefore, the sensible heat transfer at the liquid–vapor interface is calculated as

$$Q_s = h_v(T_l - T_v) \tag{8}$$

where h_v is the convective vapor heat transfer coefficient [34] calculated from

$$h_v = \frac{(f_{i/2})\text{Re}_v\ \text{Pr}_v}{1 + \left[8.7(f_{i/2})^{0.5}(\text{Pr}_v - 1)\right]}\left(\frac{k_v}{D_{\text{vap}}}\right) \tag{9}$$

In Eq. (9), f_i is the friction factor at the interface between the liquid and vapor phases and is computed using the Whalley and Hewitt equation [35] as

$$f_i = f_v\left[1 + 12\left(\frac{\rho_l}{\rho_v}\right)^{1/3}\left(1 - \alpha^{0.5}\right)\right] \tag{10}$$

The parameter f_v represents the friction factor of the vapor mass flux computed using

$$\frac{2}{f_v^{0.5}} = -1.8\log\left[\frac{6.9}{\text{Re}_v} + \left(\frac{\varepsilon/D_i}{3.7}\right)^{1.11}\right] \tag{11}$$

where ε/D_i is the relative roughness of the evaporator tube.

The mass transfer rate during the change-of-phase process, appearing as a source term in the phasic continuity equations, is calculated using the following expression:

$$\dot{M} = \frac{4}{D_i}\frac{Q_{\text{flux}} - \sqrt{\alpha_v}Q_s}{i_{fg}} \tag{12}$$

The liquid film thickness and the vapor core diameter, which depend on the rate of mass transfer between the two phases, and their variation are calculated from

$$\delta_l = \frac{D_i}{2}\left(1 - \alpha_v^{0.5}\right) \tag{13}$$

$$D_{\text{vap}} = D_i - 2\delta_l \tag{14}$$

where α_v is the void fraction of the vapor phase. Several models exist for the calculation of α_v [36, 37], which depend basically on the characteristics of the two-phase flow. Because the flow regime is assumed to be of the annular type, the variation of the void fraction is calculated using the general expression suggested by Zivi [38–40] given by

$$\alpha_v = \left\{1 + e\left(\frac{1-x_f}{x_f}\right)\left(\frac{\rho_v}{\rho_l}\right) + (1-e)\left(\frac{1-x_f}{x_f}\right)\left(\frac{\rho_v}{\rho_l}\right)^{2/3}\left[\frac{1 + e\left(\frac{1-x_f}{x_f}\right)\left(\frac{\rho_v}{\rho_l}\right)}{1 + e\left(\frac{1-x_f}{x_f}\right)}\right]^{1/3}\right\}^{-1} \tag{15}$$

where e is the fraction of liquid droplets in the vapor core. It is equal to the mass flow rate of the liquid droplets divided by the total mass flow rate of liquid. Since it is assumed that there are no liquid droplets within the vapor core, the fraction of liquid droplets is zero (i.e., $e = 0$). Therefore, the void fraction equation becomes

$$\alpha_v = \frac{1}{1 + \left(\frac{1-x_f}{x_f}\right)\left(\frac{\rho_v}{\rho_l}\right)^{2/3}} \tag{16}$$

The corresponding liquid-phase volume fraction is then computed as

$$\alpha_l = 1 - \alpha_v \tag{17}$$

Friction Model

Since the flow is assumed to be one-dimensional, shear stress effects along the various layers of the fluid investigated are neglected. The only friction force accounted for is between the refrigerant and the pipe wall and is calculated using the frictional pressure drop model. In this model, the wall shear stress is computed as

$$\tau_w = -\frac{D_i}{4}\left[\frac{dP}{dZ}\right]_F \tag{18}$$

where D_i is the pipe inner diameter and $[dP/dZ]_F$ is the frictional pressure gradient, calculated using

$$\left[\frac{dP}{dZ}\right]_F = \phi_{lo}^2 \left[\frac{dP}{dz}\right]_{Lo} \tag{19}$$

In Eq. (19), ϕ_{lo} is a two-phase multiplier. Several correlations to compute ϕ_{lo} have appeared in the literature, e.g., [19, 20, 41–44]. In the model of Lockhart and Martinelli [19], the two-phase multiplier is based on the assumption that the liquid and vapor phases flow separately. Martinelli and Nelson [41] extended the correlation given in [19] to cover situations in which the pressure is above atmospheric. Gronnerud [42] and Chisholm [43] expressed the two-phase multiplier as a function of the liquid Froude number and the refrigerant mass flux, respectively. Chawla [44] developed a model that takes into consideration friction between phases in an annular flow as well as friction effects due to fluid–wall interaction. The friction model selected for the current study is the one developed by Friedel [20], in which the correlation used to compute the two-phase multiplier is given by

$$\phi_{lo}^2 = C_1 + \frac{3.24 C_2 C_3}{\mathrm{Fr}^{0.045}\mathrm{We}^{0.035}} \tag{20}$$

The coefficients C_1, C_2, and C_3 are computed as

$$C_1 = (1 - x_f)^2 + x_f^2 \frac{\rho_l f_{vo}}{\rho_v f_{lo}} \tag{21}$$

$$C_2 = x_f^{0.78}(1 - x_f)^{0.224} \tag{22}$$

$$C_3 = \left(\frac{\rho_l}{\rho_v}\right)^{0.91} \left(\frac{\mu_v}{\mu_l}\right)^{0.19} \left(1 - \frac{\mu_v}{\mu_l}\right)^{0.7} \tag{23}$$

This correlation remains applicable as long as the viscosity ratio $\mu_l/\mu_v < 1000$ and the refrigerant mass flux $\dot{G}_R < 2000\,\mathrm{kg/m^2\,s}$ [45, 46]. Moreover, the Froude (Fr) and Weber (We) numbers appearing in Eq. (20) are defined as

$$\mathrm{Fr} = \frac{\dot{G}_R^2}{g D_i \rho_h^2} \qquad We = \frac{\dot{G}_R^2 D_i}{\rho_h \sigma} \tag{24}$$

where ρ_h is the average liquid–vapor density given by

$$\rho_h = \left(\frac{x_f}{\rho_v} + \frac{1 - x_f}{\rho_l}\right)^{-1} \tag{25}$$

Finally, the pressure-drop term, $[dP/dz]_{Lo}$ appearing in Eq. (19) is computed as

$$\left[\frac{dP}{dz}\right]_{Lo} = f_{lo} \frac{2\dot{G}_R^2}{D_i \rho_l} \tag{26}$$

Flow Quality Model

To predict the evolution of the flow quality during the change-of-phase process, two approaches are considered. The equation for the flow quality in the first method is derived from energy conservation; in the second model it is derived from mass conservation. Following are descriptions of the two models developed.

Model I: Flow quality equation derived from energy conservation. Conservation of energy over the one-dimensional differential element (or control volume) shown in Figure 1*a* requires that the rate of change in the refrigerant enthalpy over the control volume be equal to the heat transfer at the element's boundary. Mathematically, this is given by Eq. (5) presented earlier.

In the finite-volume method [47], the physical domain (circular pipe in this case) is subdivided into a number of control volumes similar to the one shown in Figure 1*a*. If dx represents the thickness of the control volume, then the total heat, dQ, crossing its surface area can be expressed in terms of the heat flux and geometric parameters as

$$dQ = dSQ_w = \pi D_i \, dx \, Q_w \tag{27}$$

Using the new expression for the term dQ, Eq. (5) can be rewritten as

$$\dot{m}\left|\frac{dh}{dx}\right| = \pi D_i Q_w \tag{28}$$

The discretized form of Eq. (28) is obtained by integration over the control volume shown in Figure 1*a*. The first step in the derivation is to transform the volume integral of the convective term into a surface integral through the application of the divergence theorem. Then, expressing the specific enthalpy of the mixture in terms of the flow quality and specific enthalpies of both phases (since the thermodynamic state of the refrigerant varies between saturated liquid and saturated vapor), the discretized equation is obtained as

$$\sum_{\text{faces}} \dot{m}|[i_l + x_f(i_v - i_l)]S_f| = \pi D_i Q_w \text{ Volume}_{\text{cylinder}} \tag{29}$$

Where S_f represents the surface area of face (f) and $\text{Volume}_{\text{cylinder}}$ is the volume of the cylindrical control volume.

Model II: Flow quality equation derived from mass conservation. The second model is derived from mass conservation based on the variations of the mean liquid and vapor phase velocities that are given by [40]

$$V_v = \frac{\dot{Q}_v}{A\alpha_v} = \left(\frac{\dot{m}}{A}\right)\frac{x_f}{\alpha_v \rho_v} = \frac{\dot{G}_R x_f}{\alpha_v \rho_v} \quad V_l = \frac{\dot{Q}_l}{A\alpha_l} = \frac{\dot{m}}{A\rho_l}\left(\frac{1-x_f}{1-\alpha_v}\right) = \frac{\dot{G}_R}{\rho_l}\left(\frac{1-x_f}{1-\alpha_v}\right) \tag{30}$$

where A is the cross-sectional area of the pipe. Referring to the mass conservation equation of the liquid or vapor phase [Eq. (1)], an equation for the flow quality is derived by substituting the variables in Eq. (1) with their equivalent expressions as

given in Eqs. (12), (16), and (30). The final form of the equation is obtained as

$$\nabla.(x_f \dot{G}_R) = \frac{4}{D_i i_{fg}} \left[Q_w - \sqrt{\frac{1}{1 + \left(\frac{1-x_f}{x_f}\right)\left(\frac{\rho_v}{\rho_l}\right)^{2/3}}} Q_s \right] \tag{31}$$

The axial variation of the refrigerant flow quality depends on the rate of evaporation/condensation and on the pressure drop effects which appear in the change of the refrigerant latent heat. The differential equation is solved using the finite-volume method, with the gradient term interpolated at the control-volume faces and the source term integrated over the entire control volume.

Wall Temperature

The pipe wall temperature is not needed in the solution process because the heat flux is specified, but it is needed as an output parameter that may be documented and used for validation purposes. To be able to calculate the wall temperature, an equation for the heat transfer at the wall is needed. For steady-state analysis, the heat transfer at the inner wall of a control volume can be expressed as

$$Q_w = A h_{\text{int}} \left(T_{\text{wall}} - T_{\text{refrigerant}} \right) \tag{32}$$

where T_{wall} is the inner wall temperature, $T_{\text{refrigerant}}$ is the refrigerant temperature, A is the wall area, and h_{int} is the convective heat transfer coefficient at the inner tube wall, which can be calculated from the correlation of Chaddock and Noerager [48] as

$$h_{\text{int}} = 1.8 h_{fc} \left(\text{Bo}.10^4 + 1.5 X^{-2/3} \right)^{0.6} \tag{33}$$

In the above equation, the Lockhart-Martinelli parameter (X), the boiling number (Bo), and the single-phase liquid heat transfer coefficient (h_{fc}) of Dittus-Boelter [49] are calculated, respectively, as

$$X = \left(\frac{1-x_f}{x_f}\right)^{0.9} \left(\frac{\rho_v}{\rho_l}\right)^{0.5} \left(\frac{\mu_l}{\mu_v}\right)^{0.1} \qquad Bo = \frac{Q_w}{G_R i_{fg}} \qquad h_{fc} = 0.023 \frac{k_l}{D_i} \text{Re}_l^{0.8} \text{Pr}_l^{0.4} \tag{34}$$

As all variables become known at the end of the iterative process, Eq. (32) is used to calculate T_{wall}.

NUMERICAL MODELS AND ALGORITHMS

The two approaches for the calculation of the flow quality presented earlier, in addition to whether heat transfer at the interface between the two phases is considered, resulted in the development of four different methods and numerical algorithms for predicting the hydrodynamic and heat transfer characteristics of the one-dimensional, two-phase flow problem under consideration. In all methods, numerical predictions are obtained via a locally iterative marching-type solution algorithm. Computations are initiated by providing the necessary input data and

boundary conditions for the first control volume. The data needed, displayed schematically in Figure 2, include: refrigerant type, pipe diameter, refrigerant mass flow rate, inner tube roughness (reflecting the type of material used for the heat exchanger), wall heat flux and saturation pressure and flow quality of the refrigerant at the inlet. Computations are then performed iteratively until a converged solution is obtained at exit from the control volume. This solution is used as the inlet condition for the next control volume and computations performed. The same sequence of events is repeated until the last refrigerant droplet has either evaporated or condensed. Therefore, the algorithm terminates once the flow quality appears to be equal to one, signifying that the refrigerant has totally evaporated; or equal to zero, indicating the end of the condensation process. Therefore, the models permit the prediction of the pipe size required to achieve full evaporation/condensation of the saturated refrigerant. Brief descriptions of the various techniques are presented next, with the differences between them summarized in Table 1*a*.

Method 1

In method 1, the sensible heat transfer at the liquid–vapor interface is assumed to be zero (i.e., the liquid and vapor phases are considered to be at the same temperature), and the flow quality of the refrigerant is predicted using Model I [Eq.

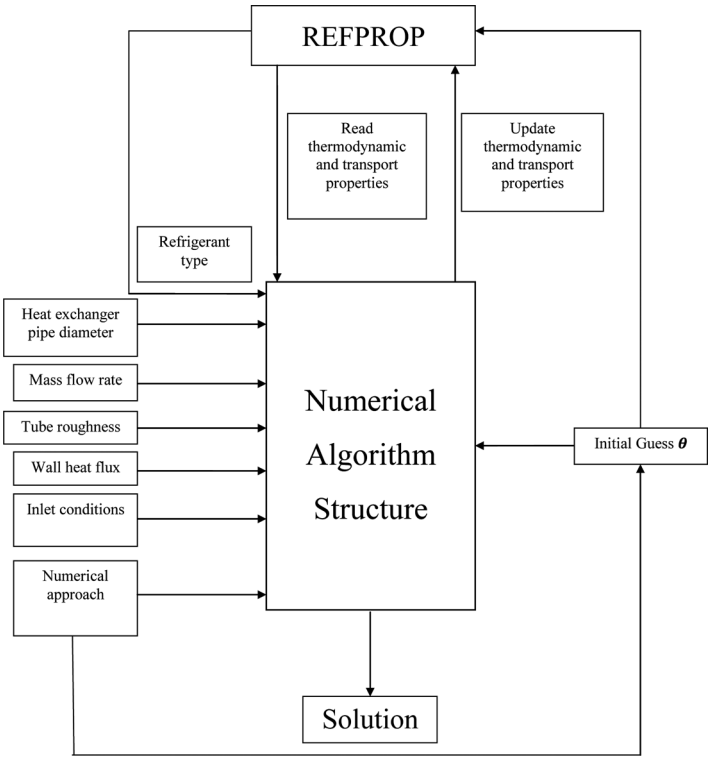

Figure 2. Algorithm showing the model inputs, initial guess vector, and interaction with REFPROP.

Table 1*a*. Description of implemented methods in terms of physical assumptions, flow quality model, and initial guess vector

Method	Physical assumption	Flow quality prediction model	Initial guess vector
1	Sensible heat transfer = 0	Proposed model	$\theta = [P]$
2	$T_l = T_v$	Derived model	$\theta = [P]$
3	Sensible heat transfer $\neq 0$	Proposed model	$\theta = [PV_v]$
4	$T_l \neq T_v$	Derived model	$\theta = [PV_v x_f]$

(29)]. By carefully examining the governing conservation equations, all model parameters are found to be functionally related to the saturation pressure. Therefore, to start the iterative process in a control volume, only the value of the saturation pressure at the control-volume outlet is needed for an initial guess. Based on the guessed saturation pressure, the thermodynamic and transport properties of the defined refrigerant are calculated using the NIST database supported by REFPROP [31]. The flow quality is calculated next from Eq. (29), the vapor volume fraction from Eq. (16), and the velocities by solving the discretized mass conservation equation of each phase. The solution proceeds by computing the wall shear stress using Eqs. (18)–(26). After this, the pressure field is updated by solving the combined momentum equation. The above steps are repeated until a converged solution is obtained. Convergence is reached when the change in the saturation pressure at the control-volume outlet between two consecutive iterations becomes smaller than a vanishing number ε_P, which is set at 10^{-5}.

Method 2

The difference between Method 2 and Method 1 is in the calculation of the flow quality, which is obtained by solving the discretized form of Eq. (31). Again, the refrigerant saturation pressure is the only variable required as an initial guess. Additional changes include the sequence in which equations are solved and the use of the mean velocity equations to compute the velocity field of each phase.

The solution starts with computing the source term of the mass conservation equations using Eq. (12), followed by computing the flow quality from the discretized form of Eq. (31). The vapor volume fraction is then calculated from Eq. (16). The solution proceeds by determining the velocity of the liquid and vapor phases using the mean velocity expressions given by Eq. (30). Finally, after estimating the wall shear stress using Eqs. (18)–(26), the refrigerant pressure is updated by solving the momentum equation (2), and convergence is checked by comparing the value of the updated pressure with its value at the previous iteration.

Method 3

In method 3, heat transfer at the interface between the two phases is assumed to occur and the flow quality is modeled using Eq. (29). Upon examining the mathematical formulation, all model variables are functionally related to two parameters, the refrigerant saturation pressure and the vapor phase-velocity.

The solution procedure starts by setting the guessed values of the saturation pressure and vapor-phase velocity at the outlet control-volume face. The volumetric coefficient of thermal expansion and the coefficient of compressibility are evaluated numerically by using Eq. (7), with variations in specific volume determined using the REFPROP [31] database. The temperatures of both phases are then computed using Eq. (6). The numerical algorithm proceeds by calculating the flow quality, the vapor-phase volume fraction, the wall shear stress, and the mass source term. Then, the continuity equations and the combined momentum equation are solved to calculate the velocity of the liquid and vapor phases, and the saturation pressure, respectively. Convergence is assumed to be reached when the changes in the values of

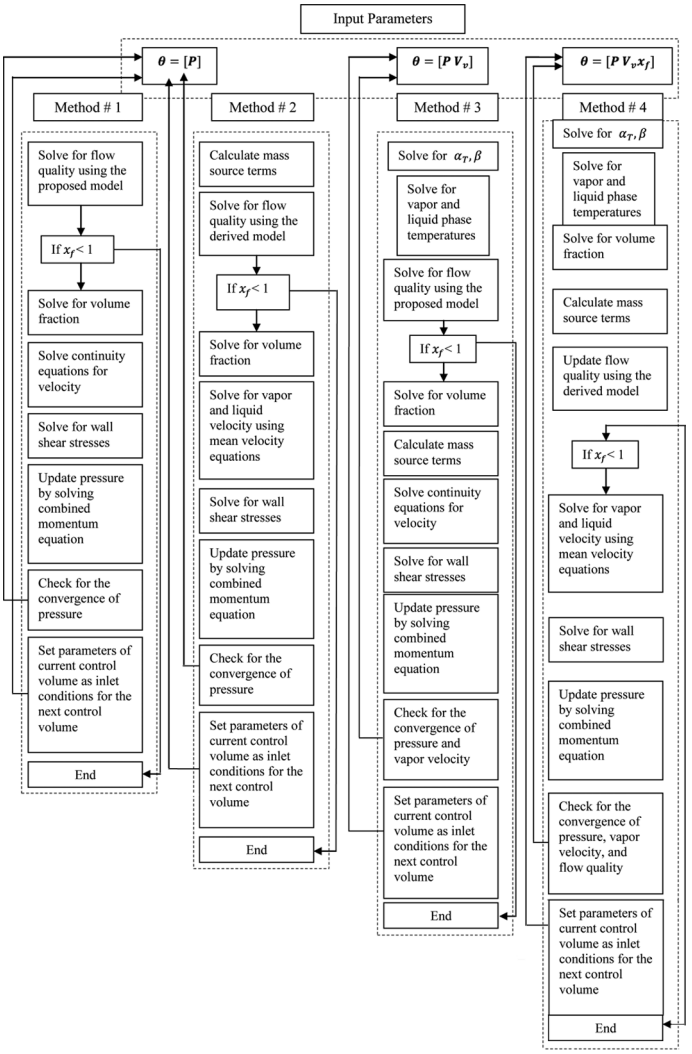

Figure 3. Numerical algorithms for the four methods.

saturation pressure and vapor velocity of two consecutive iterations become smaller than the vanishing quantities ε_P and ε_v, which are set at 10^{-5}.

Method 4

The difference between Method 4 and Method 3 is in the calculation of the flow quality which is obtained by solving the discretized form of Eq. (31). By inspecting the mathematical formulation, it is found that the model variables are functionally related to the following three parameters: the refrigerant saturation pressure, the vapor-phase velocity, and the flow quality. The detailed numerical algorithm is illustrated in Figure 3. Convergence is assumed to be reached when the changes in the values of saturation pressure, vapor velocity, and flow quality between two consecutive iterations become smaller than the vanishing quantities ε_P, ε_v, and ε_{x_f}, which are set at 10^{-5}.

Next, the effectiveness and robustness of the above numerical procedures in predicting the flow and heat transfer characteristics are assessed in terms of accuracy and computational cost.

MODEL VALIDATION

The validity of the methods developed is established by comparing the predictions obtained using these methods with the experimental measurements reported by Wattelet and Chato [50] for the evaporation of refrigerant R12 in horizontal tubes of known lengths subjected to a uniform heat flux. As depicted in Figure 4, the numerical results generated by the various techniques fall on top of each other and are indistinguishable. The figure compares numerical and experimental values of the saturation temperature (Figure 4*a*), pressure (Figure 4*b*), and flow quality (Figure 4*c*) of the refrigerant in addition to the pipe wall temperature (Figure 4*d*). In all plots, the horizontal axis represents the experimental results while the vertical axis represents the predicted results. To facilitate the comparison, lines showing the range of data spread are included in the figures, keeping in mind that the best fit is obtained when points fall along the line $y = x$. As shown in Figure 4, predictions of the saturation temperature, saturation pressure, flow quality, and wall temperature are within 20%, 17.6%, 18%, and 30% of the experimental values, respectively, In addition, the standard deviations for the parameters plotted are also included in the figures. The standard deviation of a variable x is given by the following expression:

$$\mathrm{sd} = \frac{1}{N}\sqrt{\sum_{i=1}^{i=N}\left[\frac{x_{\mathrm{predicted},i} - x_{\mathrm{experiment},i}}{x_{\mathrm{experiment},i}}\right]^2} \times 100 \tag{35}$$

The standard deviation of the saturation pressure, refrigerant bulk temperature, flow quality, and inner wall temperature from the experimental results are 0.07%, 0.012%, 4.16%, and 0.04%, respectively. All the above values compare well to similar numerical results reported in the literature [15–18, 28, 29]. Therefore, the current models are considered to predict with sufficient accuracy the flow

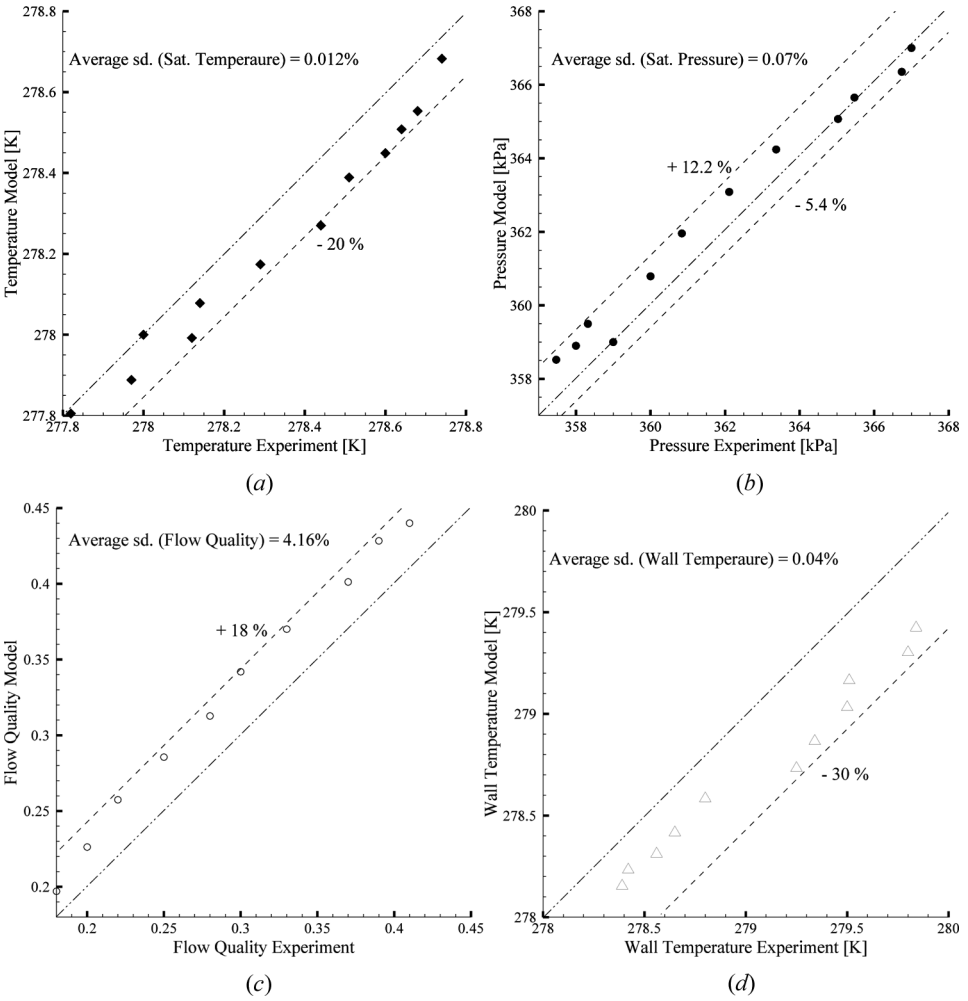

Figure 4. Comparison with the experimental data of Wattelet and Chato [50].

and heat transfer characteristics of two-phase flows undergoing evaporation/condensation processes.

BASE CASE RESULTS AND ANALYSIS

The relative performance of the four numerical methods developed is assessed in this section by generating solutions for a physical configuration denoted as the "base case" and comparing results for accuracy and computational cost. For this situation, the working refrigerant is R12 and the input parameters needed in simulating the evaporation and condensation processes are set to

Evaporation process: $D_i = 1\,\text{cm}$, $\varepsilon = 1.5 \times 10^{-6}\text{m}$, $P_{\text{sat}} = 370\,\text{kPa}$, $x_f = 0.2$, $Q_w = 10{,}000\,\text{W/m}^2$, $\dot{m} = 0.0314\,\text{kg/s}$.

Condensation process: $D_i = 1\,\text{cm}$, $\varepsilon = 1.5 \times 10^{-6}\text{m}$, $P_{\text{sat}} = 1{,}020\text{kPa}$, $x_f = 1$, $\dot{m} = 0.0314\,\text{kg/s}$.

Even though the flows in both the evaporator and condenser involve liquid and vapor phases, their dynamics are different. This is demonstrated by the results generated for the base case, which are presented in Figures 5 and 6 and are discussed next.

Numerical Limitation

As mentioned earlier, the value of the flow quality is computed at any iteration and checked to infer whether the change-of-phase process has finished (i.e., $x_f = 1$ for evaporation and $x_f = 0$ for condensation). The numerical results for the condensation phenomenon obtained with the four methods do not show any differences and, for compactness, are not compared. However, as shown in Figure 5*a*, evaporation results show discrepancies in the liquid-phase velocity of Methods 1 and 3 on one side, and Methods 2 and 4 on the other, as x_f approaches 1 (the last 4% of the evaporation process). In the results presented in Figure 4, the value of x_f did not go beyond 0.5. This is why no differences in results were obtained.

The difference between the two sets of methods lies in the way the phase velocities are calculated. In Methods 1 and 3, the liquid-phase velocity is determined by solving the discretized mass conservation equation for the liquid phase, where the term (α_l) tends to zero at the end of the evaporation process. This decrease in the value of α_l creates a numerical inaccuracy at the end (last 4%) of the evaporation process. This inaccuracy accumulates causing a nonlinear increase in the liquid velocity. Although the liquid-phase velocity is seen to be slightly overpredicted for values of x_f as low as 0.7, its dynamic effect on the saturation pressure is negligible up to $x_f = 0.96$. This is due to the fact that the liquid-phase volume fraction decreases with x_f, causing the dynamic pressure drop resulting from the change in the liquid-phase velocity to remain low [Eq. (1)] until the last stages of the evaporation process. However, proceeding with computations for values of $x_f \geq 0.96$ leads to a rapid increase

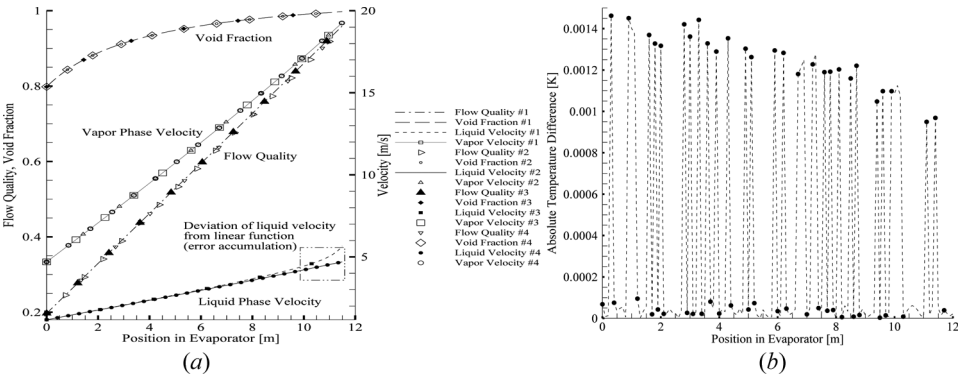

(*a*) (*b*)

Figure 5. (*a*) Comparison among the implemented methods in terms of flow quality, volume fractions, and velocity; (*b*) Absolute temperature difference of each of the liquid and vapor phases for the base case.

in the liquid-phase velocity accompanied with convergence difficulty, and eventually to an unphysical negative saturation pressure.

In Methods 2 and 4, however, the entire evaporation phenomenon is predicted accurately. Although the terms appearing in the denominator of the mean velocity expressions approach zero with the evolution of the evaporation phenomenon, simplifying the mathematical expressions of the mean velocity for the liquid and vapor phases leads to a linear function of the flow quality for small density variations. This can be written as

$$V_l = a + bx_f \tag{36}$$

where the constants a and b are given by

$$a = \frac{\dot{m}}{A\rho_l} \quad b = \frac{\dot{m}}{A\rho_l}\left[\left(\frac{\rho_l}{\rho_v}\right)^{2/3} - 1\right] \tag{37}$$

It should be clarified that density variations between the inlet and outlet conditions may reach 4%, there by causing nonlinear variations in the velocity at the end of the process. This situation should be distinguished from the case mentioned earlier, where nonlinear variation in velocity is obtained due to numerical difficulties.

The axial variation of the difference between the vapor-and liquid-phase temperatures ($|T_l - T_v|$) predicted by Methods 3 and 4 is displayed in Figure 5*b*. As depicted, the difference is marginal, indicating that heat transfer at the interface between the two phases can be neglected.

Table 1*b* presents, for each of the methods implemented, the numerical limitations and the performance prediction of the flow quality, liquid and vapor velocities, and the saturation pressure, as well as the level of accuracy and computation cost for the evaporation process.

From the previous analysis of the four approaches investigated (Table 1*b*), it is obvious that Method 2 requires the least computational cost and results in higher accuracy. Therefore, its prediction performance is graded "A." Method 4 requires a higher computational cost but gives the same level of accuracy as Method 2. Consequently, its prediction performance is graded "B." A comparison between Methods 1 and 3 shows that both methods result in the same prediction accuracy;

Table 1*b*. Percent prediction level of the implemented methods, level of accuracy, computational cost, and prediction performance for the evaporation process

	Prediction level (%)						
Method	x_f	V_v	V_l	P	Cost	Accuracy	Grade
1	96	100	96	96	Low	Low	C
2	100	100	100	100	Low	High	A
3	96	100	96	96	High	Low	D
4	100	100	100	100	High	High	B

however, the difference is in the computational cost. Therefore, the prediction performance of Method 1 is graded "C" and that of Method 3 is graded "D."

Method 2, being more accurate than Methods 1 and 3 and requiring lower computational cost than Method 4, is used to generate all results presented in the remainder of this article. The results from using other methods were also obtained and are mentioned where deemed relevant.

Evaporation Phenomenon

Evaporation results for the base case are presented in Figure 6*a*. As shown, a considerable variation in pressure during evaporation is predicted, caused by acceleration and frictional effects. The refrigerant pressure drop at the outlet is 6.8% of the inlet value, with the inlet and outlet pressures being 0.37 and 0.345 MPa, respectively (Figure 6*a*). The rapid decrease in pressure as evaporation occurs is due to the increase in the void fraction (α_v), which tends to one at the end of the process. This pressure drop greatly influences the size of the evaporator, making it dependent on several design parameters that include (1) the thermodynamic and transport properties of refrigerant used; (2) geometric (pipe diameter) and material characteristics (surface roughness); (3) the refrigerant mass flow rate; and (4) the load variation at the outer surface of the heat exchanger, which is basically affected by the heat flux gained/released during the phase-change process.

As expected, the volume fraction of the liquid phase α_l decreases in the axial direction, such that the sum of volume fractions within each control volume is equal to one. Another factor affecting pressure drop is density. The density of the liquid phase is 65 to 70 times the vapor-phase density, yielding a higher velocity distribution of the vapor phase as shown in Figure 5. These dynamic changes, in addition to wall shear stress effects, cause a decrease in the evaporation saturation pressure, which results in a decrease in the saturation temperature, or, equivalently, the refrigerant bulk temperature, and consequently, the evaporator inner wall temperature. The dark region in Figure 6*a* represents the difference between the refrigerant

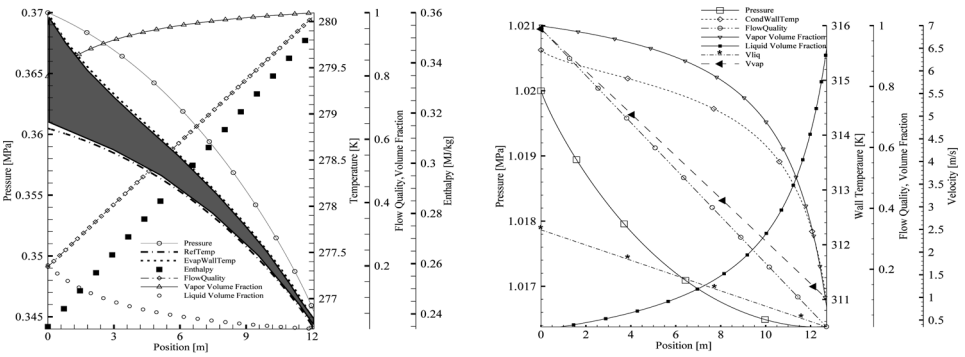

Figure 6. Variation of pressure, refrigerant and heat exchanger wall temperature, enthalpy, flow quality, volume fraction, and velocity for the base case during (*a*) evaporation and (*b*) condensation.

bulk temperature and the inner wall temperature computed from Eq. (32). It is clear that the difference decreases with the evolution of the process, and is justified by the fact that the liquid film thickness, measured along the heat exchanger wall, decreases while the convective heat transfer coefficient increases simultaneously. The end of the evaporation process is attained once the predicted value of the flow quality is one (saturated vapor). This is depicted in Figure 6*a*, which shows a linear variation of flow quality. Figure 6*a* also indicates a linear increase in the refrigerant enthalpy. This is expected, since a uniform heat flux is applied at the pipe wall. The evaporator size and capacity are estimated to be 0.36 m^2 and 3.68 kW, as predicted by Methods 1 and 3, and 0.38 m^2 and 3.959 kW as predicted by Methods 2 and 4. Table 1*c* presents a summary of the predicted results.

Condensation Phenomenon

Results presented in Figure 6*b* indicate that the end of the condensation process is realized once the predicted value of the flow quality approaches zero. As shown, the rate of decrease in pressure is higher at the beginning of the process and decreases in the axial direction, unlike the evaporation process, where the rate of decrease is higher toward the end of the process. The variation in pressure during the entire condensation process is small when compared to the pressure drop during evaporation, with the predicted decrease being around 4,000 Pa (Figure 6*b*). The formation of a liquid film at the condenser wall increases friction losses and reduces the condenser pressure. On the other hand, the heat released during condensation forces transition from a vapor phase to a liquid phase, causing a reduction in the void fraction and consequently lowering the velocity of both the vapor and liquid phases with a consequent increase in pressure. The net result of these two counteracting effects is a small decrease in pressure. Therefore, in the design of condensers, pressure drop effects can generally be neglected. Moreover, the volume fraction of the liquid phase α_l increases in the axial direction as more vapor condenses (Figure 6*b*), while α_v decreases, such that the sum of volume fractions within each control volume is equal to one. The vapor and liquid velocities, shown in Figure 6*b*, decrease linearly during the evolution of the process, where the velocity of the vapor phase approaches that of the liquid phase. Figure 6*b* further shows that the condenser wall temperature decreases as more vapor condenses. The condenser size is estimated at 0.4 m^2.

Table 1*c*. Comparison of predicted flow quality, evaporation area, and sensible heat capacity for the investigated refrigerants obtained using the four different methods

	Methods 1 and 3			Methods 2 and 4			Difference %		
Refrig. type	x_f	Area (m^2)	Capacity (kW)	x_f	Area (m^2)	Capacity (kW)	x_f	Area (m^2)	Capacity (kW)
R12	0.96	0.36	3.68	1	0.38	3.959	4%	5.5%	7%
R134a	0.96	0.48	4.854	1	0.5	5.11	4%	4.1%	5.2%
R143a	0.96	0.45	4.589	1	0.469	4.83	4%	4.2%	5.4%
R22	0.96	0.49	5.05	1	0.516	5.316	4%	5.3%	5.26%
R32	0.96	0.76	7.736	1	0.78	8.142	4%	2.6%	5.2%

PARAMETRIC INVESTIGATION

The newly developed numerical methods are used in this section to conduct a parametric study investigating the effect of refrigerant type, pipe diameter, and mass flow rate on the hydrodynamic and thermal characteristics of the flow and heat transfer fields; and on the prediction of the proper size and capacity of evaporators to ensure a total evaporation of the refrigerant.

Effect of Refrigerant Type

All model parameters are held constant, as in the base case, and evaporation solutions are generated for the following five refrigerant types: R12, R134a, R143a, R22, and R32. In all simulations, the saturation temperature at inlet is set at 5°C. Results showing the effects of thermodynamic and transport properties on the flow characteristics, size, and capacity of the evaporator are presented in Figures 7*a*–7*e*. In these figures, the horizontal axis represents the percent axial distance along the pipe normalized by the longest predicted pipe length, which is obtained with R32. Predictions obtained using R12, R134a, R143a, R22, and R32 are displayed in Figures 7*a*, 7*b*, 7*c*, 7*d*, and 7*e*, respectively. In all plots, axial variation in the flow quality, pressure, saturation temperature, wall temperature, and refrigerant enthalpy are presented. The variation in the flow quality is seen to be almost insensitive to the type of refrigerant used. Both the flow quality and enthalpy increase linearly with distance along the pipe. This is expected and is the result of the constant flux boundary condition used. The required pipe length for complete evaporation is shown to be highly dependent on the refrigerant type. This is due to the fact that different refrigerants have different latent heat of evaporation (i_{fg}). Since the same uniform heat flux value is used with the various types, the length required for a certain mass of refrigerant to evaporate is directly proportional to i_{fg}. Therefore, higher enthalpy levels are obtained with refrigerants of higher i_{fg} values. For the refrigerants investigated, the predicted size of R32 is found to be 2, 1.57, 1.68, and 1.52 times the predicted size of R12, R134a, R143a, and R22, respectively. Variations in pressure, presented in Figures 7*a*–7*e*, are nonlinear. Since the same saturation temperature is used at inlet (5°C), the corresponding inlet saturation pressures are different, resulting in pressure levels that are highly dependent on the refrigerant type. Even though R134a requires a 35% shorter pipe than R32, it results in a pressure drop (36.4 kPa) which is slightly higher than the one obtained with the latter (34 kPa). The lowest pressure drop of 18 kPa is obtained with R143a, while pressure drops with R12 and R22 are 24 and 25 kPa, respectively. As saturation temperature is directly related to saturation pressure, the largest variation in refrigerant temperature is obtained with the refrigerant for which the highest pressure drop is obtained. Therefore, variation in saturation temperature mimics variation in saturation pressure. As the heat flux is inward, the wall temperature is higher than that of the refrigerant. Moreover, the variation of the pipe wall temperature follows that of the refrigerant, with the difference between the two decreasing in the streamwise direction. The predicted evaporator area (as obtained by Method 2) varied, with the type of refrigerant used, between 0.38 m^2 and 0.78 m^2. At the same time, the capacity varied between 3.959 kW and 8.142 kW. A comparison of the sizes and capacities obtained with all methods (Methods 1–4) for the various refrigerants is presented in Table 1*c*.

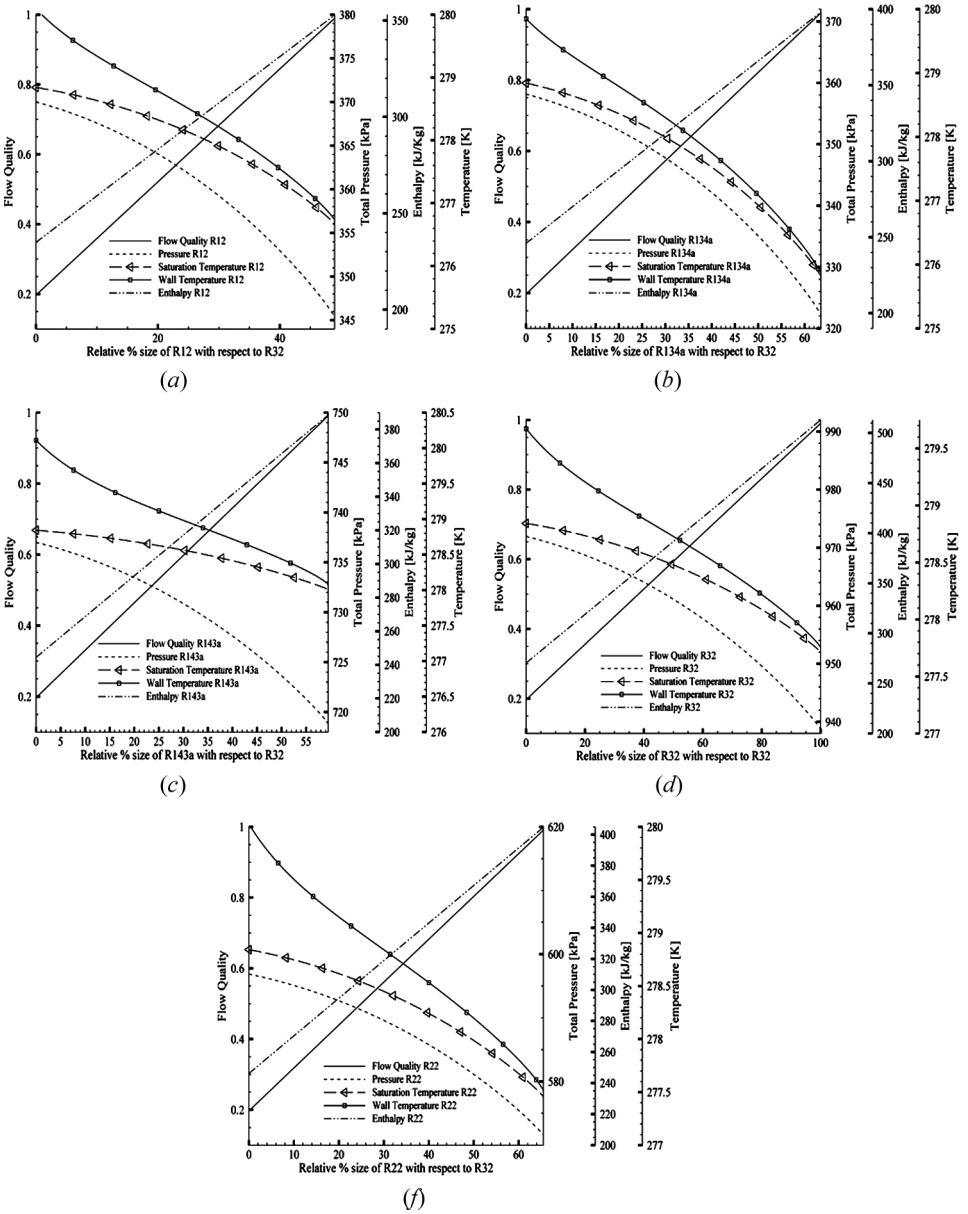

Figure 7. Variation of flow quality, pressure, enthalpy, wall and refrigerant temperatures for (*a*) R12, (*b*) R134a, (*c*) R143a, (*d*) R32, and (*e*) R22.

Variation of Pipe Diameter at Constant Mass Flux

In this section, solutions are generated by varying the refrigerant mass flow rate proportional to the pipe diameter such that the mass flux crossing the evaporator section is held constant ($\dot{G}_R = 400\text{kg/m}^2\text{s}$). The refrigerant used in the calculations

is R12, and the problem is solved for three pipe sizes of diameters $D_1 = 5$, $D_2 = 10$, and $D_3 = 15mm$, resulting in refrigerant mass flow rates of values $\dot{m}_1 = 0.0079$, $\dot{m}_2 = 0.0317$, and $\dot{m}_3 = 0.0715\,kg/s$, respectively. Predictions generated using Method 2 are displayed in Figure 8, with the horizontal axis representing the percent axial distance along the pipe normalized by the longest predicted pipe length, which is obtained with a pipe of diameter D_3. Energy conservation requires that the total heat gained through the pipe wall should be equal to the heat gained by the refrigerant to evaporate. Thus, neglecting axial variation in the latent heat of evaporation, this can be written mathematically for an evaporator of diameter D_i as

$$\pi D_i L_i Q_w = (G_R)\pi\left(D_i^2\right)/4i_{fg} \tag{38}$$

A similar equation can be written for an evaporator with a diameter D_j. Dividing the two equations, term by term, and neglecting variations in i_{fg}, an equation relating L_i and L_j is obtained as

$$\frac{L_i}{L_j} = \frac{D_i}{D_j} \tag{39}$$

The predicted lengths of the x axes plotted in Figure 8 do satisfy the above equation, as changes in i_{fg} are negligible. As shown, the computed evaporator sizes are smaller at lower values of pipe diameter and mass flow rate. The calculated pipe lengths, L_1 and L_2, are found to be equal to 66.64% and 33.35% of the length L_3, respectively.

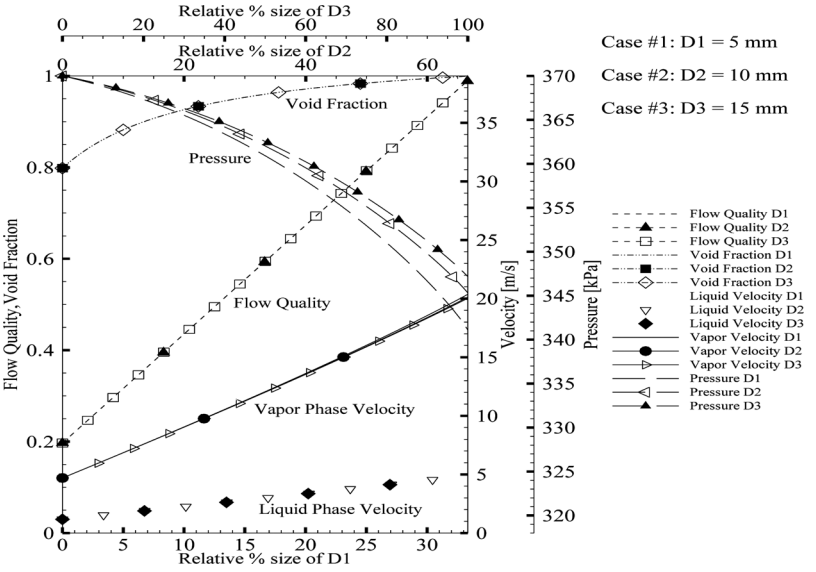

Figure 8. Variation of flow quality, void fraction, vapor and liquid-phase velocities, and pressure with mass flow rate and pipe diameter at constant mass flux.

The flow quality is shown to vary almost linearly along the pipe, and when plotted as a function of the dimensionless distance, is independent of the pipe diameter and mass flow rate. This can be shown analytically if variations in the latent heat of evaporation are neglected. Assuming one-dimensional flow with no interphase sensible heat transfer, the simplified form of Eq. (31) applicable here can be written as

$$\frac{\partial}{\partial x}(x_f G_R) = \frac{4Q_w}{D_i i_{fg}} \quad x_f = 0.2 \quad \text{at } x = 0 \tag{40}$$

The solution to the above equation (assuming i_{fg} to be constant) in a pipe of diameter D_i is given by

$$(x_f)_i = \frac{4Q_w}{D_i i_{fg} G_R} x_i + 0.2 \tag{41}$$

Because $(x_f)_i = 1$ at $x_i = L_i$, the values of the flow quality should fall along the same line when plotted using the suggested dimensionless axial distance, as obtained numerically. The void fraction being calculated using Eq. (16), and variations in the liquid and vapor densities being small, axial profiles of the void fraction for the various cases studied are expected to fall on top of each other, as predicted numerically. The same applies to liquid and vapor velocities computed using Eq. (30). The slight differences in the vapor velocity profiles at the end of the pipe are due to variations in the vapor density. Since pressure is obtained from Eq. (2), profiles shown in Figure 8 do not fall on top of each other and are dependent on the pipe diameter. The pressure drop is seen to decrease as the pipe diameter and mass flow rate increase. Results show that, compared to the case for $D_i = 5$ mm and $\dot{m} = 0.0079$, the pressure drop is lower by 14.8% for $D_i = 10$ mm and $m = 0.0317$ kg/s; and by 21.1% for $D_i = 15$ mm and $\dot{m} = 0.0715$ kg/s).

Effect of Varying the Refrigerant Mass Flow Rate at Constant Pipe Diameter

In this section, the effect of varying the mass flow rate while holding the pipe diameter constant on the hydrodynamic and thermal fields during refrigerant evaporation is investigated. Four mass flow rates, $\dot{m}_1, \dot{m}_2, \dot{m}_3,$ and $\dot{m}_4$, are considered such that $\dot{m}_4 = \frac{4}{3}\dot{m}_3 = 2\dot{m}_2 = 4\dot{m}_1$, with the largest mass flow rate considered the reference case to which other predictions are compared ($\dot{m}_4 = 0.0628$kg/s). Simulation results using Method 2 are depicted in Figure 9.

Similar to earlier results, the horizontal axis represents the percent axial distance along the pipe normalized by the longest predicted pipe length, which is obtained with a mass flow rate of value $\dot{m}_4$. Using arguments similar to those presented earlier, it can easily be shown that the relation between pipe lengths L_i and L_j obtained with mass flow rates $\dot{m}_i$ and $\dot{m}_j$ should satisfy

$$\frac{L_i}{L_j} = \frac{\dot{m}_i}{\dot{m}_j} \tag{42}$$

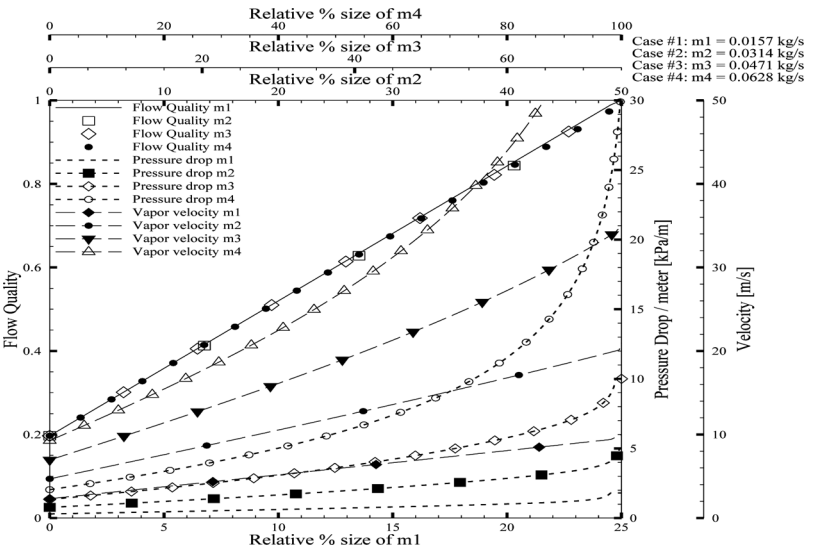

Figure 9. Effect of splitting the refrigerant mass flow rate on the flow quality, pressure drop, and vapor velocity in evaporators.

The numerical values obtained satisfy the above equation ($L_1 = 0.25L_4$, $L_2 = 0.5L_4$, and $L_3 = 0.75L_4$). Again, an analytical equation for the flow quality can be derived, as was done previously, and is given by

$$(x_f)_i = \frac{\pi D_i Q_w}{i_{fg} m_i} x_i + 0.2 \tag{43}$$

Numerically, almost a linear variation for the flow quality is obtained (Figure 9), and when plotted as a function of the dimensionless axial distance, almost all values fall along the same line. The slight differences are due to variation in i_{fg} values which are neglected in the analytical solution.

As the vapor velocity is proportional to the mass flow rate [Eq. (30)], its level increases as the mass flow rate increases. Numerical results displayed in Figure 9 reflect this behavior, with vapor velocity profiles being higher at higher mass flow rates. At a given mass flow rate, the axial variation in the vapor velocity is described by Eq. (30). Substituting the void fraction given by Eq. (16) into Eq. (30), the vapor velocity can be rewritten as

$$V_v = \left(\frac{\dot{m}}{A}\right) \frac{1}{\rho_v} \left[x_f + (1 - x_f) \left(\frac{\rho_v}{\rho_l}\right)^{2/3} \right] \tag{44}$$

This shows that if variations in density are negligible, then the vapor velocity will be directly proportional to the flow quality. Since x_f increases linearly with distance along the pipe, then V_v should also increase linearly with distance. This linear behavior in the variation of V_v is obtained at low mass flow rates

Table 2*a*. Comparison of pressure drop and enthalpy at different mass flow rates

	$\dot{m}$	h_{in} (kJ/kg)	h_{out} (kJ/kg)	$\frac{h_{out}-h_{out,ref}}{h_{out,ref}}$	P_{in} (Pa)	P_{out} (Pa)	(Pa)	$\Delta P/\Delta P_{ref}$
m_1	25%	234.904	353.562	+2.7%	370,000	365,646	4,354	2.2%
m_2	50%	234.904	352.805	+2.5%	370,000	345,405	24,595	13.15%
m_3	75%	234.904	350.844	+1.93%	370,000	299,038	70,962	37.36%
m_4	Ref.	234.904	344.190	Ref.	370,000	180,185	189,815	Ref.

($\dot{m}_1$ and $\dot{m}_2$). Departure from the linear variation (Figure 9) starts to appear for the case when the mass flow rate is $\dot{m}_3$ and is clearly evident at the largest mass flow rate considered ($\dot{m}_4$). This nonlinear behavior is also obtained with x_f at high mass flow rates and is due to important variations in density that are no longer negligible. These variations in density are due to important variations in pressure caused by the large pressure drops at higher velocities. As shown in Figure 9, variations in the pressure gradients are much higher at higher mass flow rates. Computed values of pressure at exit are reported in Table 2*a*. Although changes in pressure are negligible at low mass flow rates, the outlet pressure is less than half the inlet value at the highest mass flow rate considered. The pressure drops for cases 1–3 (Table 2*a*), are 2.2%, 13.15%, and 37.36% of the pressure drop obtained at the highest mass flow rate considered. Table 2*a* also indicates that the specific enthalpy of the refrigerant at outlet decreases as the mass flow rate is increased. The percent difference in the total energy at outlet for cases 1–3 (Table 2*a*), are 2.7%, 2.5%, and 1.93% higher than the total energy obtained at the highest mass flow rate considered.

This last result suggests that the performance of an evaporator operating at a certain refrigerant mass flow rate can be optimized in terms of capacity and pressure drop by splitting the flow to pass through two or more pipes instead of only one. This is demonstrated by comparing the performance of a single-pipe heat exchanger with the performance achieved by using two, three, and four pipes for the same total mass flow rate. The original configuration is considered to be the "reference case," composed of one pipe in which the largest mass flow rate is flowing ($\dot{m}_4$). The second heat exchanger is composed of two pipes with different mass flow rates ($\dot{m}_3$ and $\dot{m}_1$). The third heat exchanger is also composed of two pipes with equal mass flow rates ($\dot{m}_2$). The fourth heat exchanger is composed of four pipes with equal mass flow rates ($\dot{m}_1$). In all cases the total mass flow rate is equal to $\dot{m}_4$. Table 2*b* presents the predicted heat exchanger sizes and capacities. The four-pipe heat exchanger yielded an increase of 9% in capacity and a reduction of 5.2% in the total size

Table 2*b*. Comparison of predicted evaporator size and capacity for different numbers of pipes

Coil	m_1	m_2	m_3	m_4	Size1 (m^2)	Size2 (m^2)	Size3 (m^2)	Size4 (m^2)	Total size (m^2)	Size red. (%)	Cap. (kW)	% Diff. capacity
1				x				0.76	0.76	Ref.	6.83	Ref.
2	x		x		0.18		0.56		0.74	2.6%	7.32	+7.1%
3		2x				2*0.38			0.76	0	7.4	+8.3%
4	4x				4*0.18				0.72	5.2%	7.45	+9%

compared to the reference case. With respect to the reference case, the total capacities of the second and third heat exchangers are increased by 7.1% and 8.3%, while their sizes are reduced by 2.6% and 0%, respectively. It should be mentioned that, with the current formulation, the capacity is expected to increase as the number of pipes increases. This is due to the fact that the effects of the air side are neglected.

CLOSING REMARKS

The current study presented a new numerical approach for predicting the hydrodynamic and thermal fields of pure refrigerants during change-of-phase processes. The model accounts for the variability in thermodynamic and transport properties of refrigerants resulting from dynamic and frictional pressure gradients. Two methodologies to calculate the flow quality were tested. In the first, an equation for x_f is obtained from mass conservation, while in the second an equation is derived from energy conservation. Both approaches yield similar results. Moreover, four control-volume–based numerical methods, denoted Methods 1 through 4, for calculating the flow and heat transfer fields were implemented; and their limitations, mathematical formulations, and prediction performances were clearly demonstrated. Methods 1 and 3 are capable of predicting up to 96% of the evaporation process. Method 2 had the best prediction performance, with lower computational cost and higher accuracy. Method 4 achieved the same level of accuracy as Method 2; however, it required a higher computational cost. The accuracy of predictions was established by direct comparison with measurements. The new approach was used to analyze the effect of refrigerant type, pipe diameter, and mass flow rate on the flow and heat transfer characteristics in evaporators. For a given refrigerant mass flow rate, results suggested that it is more efficient to use a multipipe heat exchanger than a singlepipe of equal diameter.

REFERENCES

1. D. Z. Guo, D. L. Sun, Z. Y. Li, and W. Q. Tao, Phase Change Heat Transfer Simulation for Boiling Bubbles Arising from a Vapor Film by the VOSET Method, *Numer. Heat Transfer A*, vol. 59, pp. 857–881, 2011.
2. R. S. Maurya, S. V. Diwakar, T. Sundararajan, and S. K. Das, Numerical Investigation of Evaporation in the Developing Region of Laminar Falling Film Flow under Constant Wall Heat Flux Conditions. *Numer. Heat Transfer A*, vol. 58, pp. 41–64, 2010.
3. C. Kunkelmann and P. Stephan, CFD Simulation of Boiling Flows Using the Volume-of-Fluid Method within Open FOAM. *Numer. Heat Transfer A*, vol. 56, pp. 631–646, 2009.
4. H. G. Hu and C. Zhang, A New Inundation Correlation for the Prediction of Heat Transfer in Steam Condensers. *Numer. Heat Transfer A*, vol. 54, pp. 34–46, 2008.
5. W. Lee and G. Son, Bubble Dynamics and Heat Transfer during Nucleate Boiling in a Microchannel. *Numer. Heat Transfer A*, vol. 53, pp. 1074–1090, 2008.
6. Y. Zhang, X. F. Peng, and I. Conte, Heat and Mass Transfer with Condensation in Non-saturated Porous Media. *Numer. Heat Transfer A*, vol. 52, pp. 1081–1100, 2007.
7. H. Louahlia-Gualous and M. Asbik, Numerical Modeling of Annular Film Condensation inside a Miniature Tube. *Numer. Heat Transfer A*, vol. 52, pp. 251–273, 2007.

8. S. Bin-Mansoor and B. S. Yilbas, Laser Pulse Heating of Steel Surface: Consideration of Phase-Change Process. *Numer. Heat Transfer A*, vol. 50, pp. 787–807, 2006.
9. H. Louahlia-Gualousand and L. El Omari, Local Heat transfer for the Evaporation of a Laminar Falling Liquid Film on a Cylinder: Experimental, Numerical, and Inverse Heat Conduction Analysis. *Numer. Heat Transfer A*, vol. 50, pp. 667–688, 2006.
10. M. Asbik, O. Ansari, and B. Zeghmati, Numerical Study of Boundary-Layer Transition in Flowing Film Evaporation on Horizontal Elliptical Cylinder. *Numer. Heat Transfer A*, vol. 48, pp. 645–669, 2005.
11. A. Abdul-Razzak, M. Shoukri, and J. S. Chang, Measurement of Two-Phase Refrigerant Liquid-Vapor Mass Flow Rate—Part III: Combined Turbine, and Venturi Meters, and Comparison with Other Methods, *ASHRAE Trans. Res.*, vol. 101, pp. 532–538, 1995.
12. M. M. Awad and Y. S. Muzychka, *Bounds on Two-Phase Flow Part I—Frictional Pressure Gradient in Circular Pipes, ASME International Mechanical Engineering Congress and Exposition, paper # IMECE2005–81543*, Orlando, FL, November 5–11, 2005.
13. J. Solberg, N. R. Miller, and P. Hmjak, *A Sensor for Estimating the Liquid Mass Fraction of the Refrigerant Exiting an Evaporator, SAE 2000 World Congress*, Paper#2000–01-0976, Detroit, MI, March 6–9, 2000.
14. Y. C. Kim and D.L. O'Neal, The Effect of Oil on the Two-Phase Critical Flow of Refrigerant 134a through Short Tube Orifices, *Int. J. Heat Mass Transfer*, vol. 37, pp. 1377–1385, 1994.
15. W. Sripattrapan and S. Wongwises, Two-Phase Flow of Refrigerants during Evaporation under Constant Heat Flux in a Horizontal Tube. *Inte. Commun. Heat Mass Transfer*, vol. 32, pp. 386–402, 2006.
16. A. Greco and G. P. Vanoli, Experimental Two-Phase Pressure Gradients during Evaporation of Pure and Mixed Refrigerants in a Smooth Horizontal Tube: Comparison with Correlations. *Int. J. Heat Mass Transfer*, vol. 42, pp. 709–725, 2006.
17. A. Greco and G. P. Vanoli, Evaporation of Refrigerants in a Smooth Horizontal Tube: Prediction of R22 and R507 Heat Transfer Coefficients and Pressure Drop. *Appl. Thermal Eng.*, vol. 24, pp. 2189–2206, 2004.
18. A. Greco and G. P. Vanoli, Flow Boiling Heat Transfer with HFC Mixtures in a Smooth Horizontal Tube Part I: An Experimental Investigation, *Exp. Thermal Fluid Sci.*, vol. 29, pp. 189–198, 2005.
19. R. W. Lockhart and R. C. Martinelli, Proposed Correlation of Data for Isothermal Two-Phase Two-Component Flow in Pipes, *Chem. Eng. Prog.*, vol. 45, pp. 39–45, 1949.
20. L. Friedel, Improved Friction Pressure Drop Correlation for Horizontal and Vertical Two-Phase Pipe Flow. European Two-Phase Flow Group Meeting, Paper E2, Ispra Italy, June 1979.
21. J. C. Chen, Correlation for Boiling Heat-Transfer to Saturated Fluids in Convective Flow, *Ind. Eng. Chem. Process Design Devel.*, vol. 5, pp. 322–339, 1966.
22. K. E. Gungor and R. H.S. Winterton, A General Correlation for Flow Boiling in Tubes and Annuli, *Int. J. Heat Mass Transfer*, vol. 29, pp. 351–358, 1986.
23. S. G. Kandlikar, A General Correlation for Saturated Two-Phase Flow Boiling Heat-Transfer inside Horizontal and Vertical Tubes. *J. Heat Transfer*, vol. 112, no. 1, pp. 219–228, 1990.
24. M. Shah, A New Correlation for Heat-Transfer during Boiling Flow through Pipes, *ASHRAE Trans.*, vol. 82, no. 2, pp. 66–86, 1976.
25. S. Yoshida, H. Mari, H. Hong, and T. Matsunaga, Prediction of Binary Mixture Bowling Heat Transfer Coefficient Using Only Phase Equilibrium Data. *Trans. JAR*, vol. 11, pp. 67–78, 1994.
26. J.-T. Oh, A. S. Pamitran, K.-I. Choi, and P. Hrnjak, Experimental Investigation on Two-Phase Flow Boiling Heat Transfer of Five Refrigerants in Horizontal Small Tubes

of 0.5, 1.5, and 3.0 mm Inner Diameters, *Int. J. Heat Mass Transfer*, vol. 54, pp. 2080–2088, 2011.
27. Z. Yang, X. F. Peng, and P. Ye, Numerical and Experimental Investigation of Two Phase Flow during Boiling in a Coiled Tube. *Int. J. Heat Mass Transfer*, vol. 51, pp. 1003–1016, 2008.
28. A. S. Dalkilic, Condensation Pressure Drop Characteristics of Various Refrigerants in a Horizontal Smooth Tube. *Int. Commun. Heat Mass Transfer*, vol. 38, pp. 504–512, 2011.
29. P. Bhramara, V. D. Rao, K. V. Sharma, and T. K.K. Reddy, CFD Analysis of Two Phase Flow in a Horizontal Pipe—Prediction of Pressure Drop, *Int. J. Aerospace Mech. Eng.*, vol. 3, no. 2, pp. 72–78, 2009.
30. E. Granryd, Optimum Circuit Tube Length, and Pressure Drop on the Refrigerant Side of Evaporators, Proceedings of the International Refrigeration Conference, Purdue University, West Lafagetle, IN, 1992.
31. E. W. Lemmon, M. L. Huber, and M. O. McLinden, NIST Reference Fluid Thermodynamic and Transport Properties—REFPROP, Version 8, User's Guide, Computer Software, U.S. Department of Commerce, Technology Administration, National Institute of Standards and Technology, Gaithersburg, MD, April, 2007.
32. P. M. Morse, *Thermal Physics*, rev. ed., W. A. Benjamin, New York, 1964.
33. R. Viswanathan and E. S. Rajagopal, On the Exact Relation between C_p and C_v in Crystalline Media. *Physica*, vol. 27, pp. 1226–1228, 1961.
34. L. Prandtl, *Fuehrer durch die Stroemungslehre, Vieweg und Sohn*, Braunschweig, Germany, 1944.
35. P. B. Whalley and G. F. Hewitt, The Correlation of Liquid Entrainment Fraction and Entrainment Rate in Annular Two-Phase Flow, UKAEA Rep. AERE-R9187, 1978.
36. Z. Rouhaniand, E. Axelsson, Calculation of Void volume Fraction in the Subcooled and Quality Boiling Regions, *Int. J. Heat Mass Transfer*, vol. 13, pp. 383–393, 1970.
37. A. A. Armand, The Resistance during the Movement of a Two-Phase System in Horizontal Pipes, *Izvestiya Vsesoyuznogo Teplotekhnicheskogo Instituta*, vol. 1, pp. 16–23, 1946.
38. S. M. Zivi, Estimation of Steady-State Steam Void-Fraction by Means of the Principle of Minimum Entropy Production, *ASME J. Heat Transfer*, vol. 86, pp. 247–252, 1975.
39. D. Chisholm, Pressure Gradients due to Friction during the Flow of Evaporating Two-Phase Mixtures in Smooth Tubes and Channels, *Int. J. Heat Mass Transfer*, vol. 16, pp. 347–358, 1973.
40. *Engineering Data Book III, Void fractions in two-phase flow*, Wolverine Tube, Inc., pp. 17.1–17.33, 2006.
41. J. R.S. Thom, Prediction of Pressure Drop during Forced Circulation Boiling of Water, *Int. J. Heat Mass Transfer*, vol. 7, pp. 709–724, 1964.
42. R. Grönnerud, Investigation of Liquid Hold-up, Flow Resistance and Heat Transfer in Circulation Type Evaporators, Part IV: Two-Phase Flow Resistance in Boiling Refrigerants, Annexe 1972–1, Bulletin de l'Institute du Froid, 1979.
43. D. Chisholm, Pressure Gradients due to Friction during the Flow of Evaporating Two-Phase Mixtures in Smooth Tubes and Channels, *Int. J. Heat Mass Transfer*, vol. 16, pp. 347–358, 1973.
44. J. M. Chawla, Warmeubergang und Druckabfall in waagerechten Rohrenbei der Stromung von verdampfenden Kaltemitteln, VDI-Forschungs heft 523, 1967.
45. P. B. Whalley, *Boiling, Condensation, and Gas-Liquid Flow*, Clarendon Press, Oxford, MK, 1987.
46. *Engineering Data Book III, Two-phase pressure drops*, Wolverine Tube, Inc., pp. 13.1–13.34, 2006.
47. S. V. Patankar, *Numerical Heat Transfer and Fluid Flow*, Hemisphere, New York, 1981.

48. J. B. Chaddock and J. A. Noerager, Evaporation of Refrigerant 12 in a Horizontal Tube with Constant Wall Heat Flux, *ASHRAE Transactions*, vol. 72, pp. 90–102, 1966.
49. A. Jokar, M. H. Hosni, and S. J. Eckels, Dimensional Analysis on the Evaporation and Condensation of Refrigerant R-134a in Minichannel Plate Heat Exchangers, *Appl. Thermal Eng.*, vol. 26, pp. 2287–2300, 2006.
50. J. P. Wattelet, and J. C. Chato, *Design, Building, and Baseline Testing of an Apparatus Used to Measure Evaporation Characteristics of Ozone-Safe Refrigerants*, Air Conditioning and Refrigeration Center, The University of Illinois at Urbana-Champaign, ACRC-TR-90–02, 1990.